

Thesis Title

A subtitle of your thesis

Author name



Thesis submitted for the degree of
Master in Master's Program Name <change at
main.tex>
60 credits

Department Name <change at main.tex>
Faculty name <change in duoforside.tex>

UNIVERSITY OF OSLO

Spring 2022

Thesis Title

A subtitle of your thesis

Author name

© 2022 Author name

Thesis Title

<http://www.duo.uio.no/>

Printed: Reprosentralen, University of Oslo

Abstract

Contents

1	Introduction	1
I	Theory	3
2	High-Entropy alloys	4
2.1	Fundamentals	4
2.2	Core effects and properties	7
3	Modeling of random alloys	9
3.1	The Special Quasi-random Structure model	9
3.1.1	Mathematical description	10
3.1.2	Applications to high-entropy alloys	12
4	Density Functional Theory	16
4.1	Review of Quantum Mechanics	17
4.1.1	The Shrodinger equation	17
4.1.2	Approximations to the many-body Shrodinger equation	18
4.2	Kohn-Sham density functional theory	20
4.2.1	Density functional theory	20
4.2.2	The Kohn-Sham Equation	21
4.3	Limitations of DFT - Insert refs	22
II	Methodology and Implementation	24
5	Practical application of DFT	25
5.1	The Exchange-Correlation functional	25
5.1.1	Local density approximation	25
5.1.2	Generalized gradient approximation	26
5.1.3	Meta-GGA	26
5.1.4	Hybrid functionals	27
5.1.5	Outlook	27
5.2	Fundamental aspects of practical DFT calculations	28
5.3	Self-consistent field calculation	30

6	Computational details	32
6.1	Vienna Ab initio Simulation Package	32
6.2	Generation of SQS	34
6.3	Utility scripts	35
III	Results and Discussion	37
7	The results of eqvimolar (CrFeMnNi)Si₂ in the β-FeSi₂ structure	39
7.1	The band gap	41
7.2	Local and projected density of states	44
7.3	Results from SCAN and HSE06 functionals	46
7.4	Pair distribution functions	52
7.5	SQS size	54
8	Permutations of (CrFeMnNi)Si₂	58
9	Different compositions and crystal structure	63
9.1	New compositions	63
10	Overview and outlook	65
10.1	Literature	65
10.2	General thoughts	66
10.3	Other things	70
10.4	Cr ₄ Fe ₄ Mn ₄ Ni ₄ Si ₃₂ in different crystal structures	73
10.5	Overview	75
IV	Conclusion	76
A	Compositions	73
A.1	Projected density of states	73
A.2	Probability distribution functions	76
B	Eqvimolar alloy	78
B.1	DOS	78
C	Charge density	80

List of Figures

2.1	Formation of HEA based on δ and N . Figures adopted from [hea2016_ch2]	6
2.2	A schematic illustration of lattice distortion in high-entropy alloys. Figure from [owen_jones_2018]	8
3.1	PDFs of (a) 20 and (b) 250 atom SQS models of CrFeMnNi [hea2016_ch10]	13
3.2	Density of states with SQS and MC/MD of FCC CoCrFeNi, figure from [hea2016_ch10]	14
3.3	Probability distribution functions with SQS and MC/MD of HCP CoOsReRu [hea2016_ch10]	14
4.1	Number of DFT studies per year from 1980 to 2021 [dimensions].	16
5.1	Calculated to experimental band gap measurements of Becke-Johnsoon, modified Becke-Johnson and SCAN functionals [xc_benchmark]	27
5.2	Self consistent iteration of a DFT calculation. Figure adopted from lecture notes fys-mena4111 cite	31
6.1	48 atom SQS based on eqvimolar distribution of Cr, Fe, Mn and Ni in and $FeSi_2$ cell.	36
7.1	Density of states of SQS D (CrFeMnNi)Si ₂ with PBE.	41
7.2	Density of states of SQS B (CrFeMnNi)Si ₂ with PBE.	41
7.3	Local density of states of Si (SQS D)	44
7.4	Local density of states of (a) Cr, (b) Mn, (c) Fe, (d) Ni in SQS D.	44
7.5	Projected density of states SQS D CFMN (fesi2) from PBE calculation	45
7.6	Projected density of states of SQS D and B around E_F	45
7.7	Density of states illustrating the band gaps from PBE and SCAN calculations for SQS E and D.	47
7.8	Density of states of SQS B with HSE06	48
7.9	Something	48
7.10	Probability distribution function of SQS D (top) and B (bottom)	52
7.11	CPU time, Make log plot instead	54
7.12	Density of states of SQS E 192 atom SQS.	56

7.13	Pair distribution functions of SQS sizes (top) 48 atoms, (middle) 96 atoms, (bottom) 192 atoms	57
8.1	Projected density of states of (a) $\text{Cr}_3\text{Fe}_3\text{Mn}_7\text{Ni}_3\text{Si}_{32}$ (SQS B), (b) $\text{Cr}_5\text{Fe}_5\text{Mn}_3\text{Ni}_3\text{Si}_{32}$ (SQS C), (c) $\text{Cr}_5\text{Fe}_3\text{Mn}_5\text{Ni}_3\text{Si}_{32}$ (SQS A), (d) $\text{Cr}_3\text{Fe}_5\text{Mn}_5\text{Ni}_3\text{Si}_{32}$ (SQS D)	61
8.2	Projected density of states of $\text{Cr}_3\text{Fe}_3\text{Mn}_3\text{Ni}_7\text{Si}_{32}$ around E_F	62
9.1	Projected density of states of $(\text{CrFeMnCo})\text{Si}_2$	65
9.2	Density of states of a) $(\text{CrFeCoNi})\text{Si}_2$ and b) $(\text{CrFeTiNi})\text{Si}_2$	66
9.3	Density of states of two SQSs of $(\text{CoFeMnNi})\text{Si}_2$	66
A.1	$\text{chCr}_4\text{Fe}_4\text{Co}_4\text{Ni}_4\text{Si}_{32}$	73
A.2	$\text{chCo}_4\text{Fe}_4\text{Mn}_4\text{Ni}_4\text{Si}_{32}$	74
A.3	$\text{chCr}_4\text{Fe}_4\text{Mn}_4\text{Co}_4\text{Si}_{32}$	74
A.4	$\text{chCr}_4\text{Fe}_4\text{Ti}_4\text{Ni}_4\text{Si}_{32}$	75
A.5	$\text{chCr}_4\text{Fe}_4\text{Mn}_4\text{Ti}_4\text{Si}_{32}$	75
A.6	Probability distribution functions of top: $\text{Co}_4\text{Fe}_4\text{Mn}_4\text{Ni}_4\text{Si}_{32}$ (SQS D), middle: $\text{Cr}_4\text{Fe}_4\text{Co}_4\text{Ni}_4\text{Si}_{32}$ (SQS B), bottom: $\text{Cr}_4\text{Fe}_4\text{Mn}_4\text{Co}_4\text{Si}_{32}$ (SQS B)	76
A.7	Probability distribution function of top: $\text{Cr}_4\text{Fe}_4\text{Mn}_4\text{Ti}_4\text{Si}_{32}$ (SQS B), bottom: $\text{Cr}_4\text{Fe}_4\text{Ti}_4\text{Ni}_4\text{Si}_{32}$ (SQS B))	77
B.1	Density of states SQS A $(\text{CrFeMnNi})\text{Si}_2$ with PBE.	78
B.2	Density of states SQS E $(\text{CrFeMnNi})\text{Si}_2$ with PBE.	79

List of Tables

7.1	Total energy per atom, final magnetic moment and band gap of 5 unique SQS of (CrFeMnNi)Si ₂ based on the β -FeSi ₂ unit cell.	40
7.2	Band gap of the 5 SQSs of (CrFeMnNi)Si ₂ calculated from the eigenvalues in spin up, down and total.	42
7.3	Band gap of SQS D as a function of occupancy in the eigenvalues.	43
7.4	Band gap calculated with PBE, SCAN and HSE06 XC-functionals of (CrFeMnNi)Si ₂ SQSs.	46
7.5	Minimum gap between k-point in valence band and conduction band in SQS B from PBE, SCAN and HSE06	49
7.6	Band gap from HSE06 calculations with gaussian smearing and smearing width <i>sigma</i> equal to 0.05 and 0.005, and the tetrahedron method (TBC). "-" mean unchanged values, "ND" means not done.	50
7.7	Overview 48, 96 and 192 SQSs.	54
7.8	Band gap of SQSs of 48, 96 and 192 atoms each of (CrFeMnNi)Si ₂ . The names are arbitrary, ie A in 48 does not equal A in 96 or 192.	55
8.1	Summary composition diagram	58
8.2	Band gaps of various compositions of (CrFeMnNi)Si ₂ . Most stable SQS of a set is highlighted in bold text, band gap with defect states are listed in cursive. Some SQSs were excluded from the table due to unsuccessful calculations.	60
9.1	Overview new compositions	63
9.2	Final magnetic moment of the most stable supercell of each composition.	64
9.3	Band gaps of the most stable SQS of β -FeSi ₂ high-entropy silicide compositions as a function of occupancy in the eigenvalues.	65
10.1	Mean and standard deviation of the total energy and magnetic moment per atom, plus enthalpy of formation of the listed mean energies (FeSi ₂).	68

10.2 Total and spin dependent band gap of 4 permutations of CFMN (fesi2) with PBE GGA calculation. The structures that are excluded from this list either failed in calculations, or does not show any band gap.<	70
---	----

Preface

Chapter 1

Introduction

some introduction on the importance of discovering new materials and alloying.

Need something on thermoelectricity related to both the band gap and high-entropy alloys.

High-entropy alloys is a novel class of materials based on alloying multiple components, as opposed to the more traditional binary alloys. This results in an unprecedented opportunity for discovery of new materials with a superior degree of tuning for specific properties and applications. Recent research on high-entropy alloys have resulted in materials with exceedingly strong mechanical properties such as strength, corrosion and temperature resistance, etc **find references**. Meanwhile, the functional properties of high-entropy alloys is vastly unexplored. In this study, we attempt to broaden the knowledge of this field, the precise formulation of this thesis would be an exploration on the possibilities of semiconducting high-entropy alloys.

A key motivation of this thesis is the ability to perform such a broad study of complex materials in light of the advances in material informatics and computational methods. In this project, we will employ Ab initio methods backed by density functional theory on top-of the line supercomputers and software. 20 years ago, at the breaking point of these methods, this study would have been significantly narrower and less detailed firstly, but secondly would have totaled ... amount of CPU hours to complete (**Calculate this number**). In the addition to the development in computational power, is also the progress of modeling materials, specifically we will apply a method called Special Quasi-random Structures (SQS) to model high-entropy alloys or generally computationally complex structures. Together with the open landscape of high-entropy alloys described above, these factors produce a relevant study in the direction of applying modern computational methods to progress the research of a novel material class and point to promising directions for future research.

In specifics, this thesis revolve around the electrical properties of high-entropy alloys, mainly the band gap as this is the key indicator for a semiconducting material and it's applicability. Semiconductors are the building blocks in many different applications in today's world, ranging

from optical and electrical devices, to renewable energy sources such as solar and thermoelectricity. Given the economic and sustainable factors concerning silicon, in addition to its role in relevant applications such as microelectronics and solar power. Silicon emerges as a natural selection to build our alloys around. Furthermore, the development and research on both high entropy alloys and metal silicides have been heavily centered around 3d transition metals. Keeping in line with the economic and environmental factors, we will continue this direction by focusing on high entropy stabilized sustainable and economic 3d metal silicides **Not happy with this writing**. Throughout the study we will analyze a great number of permutations of 3d silicides, from different initial metal silicides such as $CrSi_2$, $FeSi_2$, $MnSi_{1.75}$, Fe_2Si , each with distinct properties relating to the band gap, crystal structure and metal to silicon ratio. In addition, the permutations include numerous metal distributions and elements within the 3d-group of metals. Examples are Co, Cr, Fe, Mn, and Ni.

Given a background in high-entropy alloys, one could ask if this study is truly sensible. In the later sections we will cover the details of this field, and it quickly become clear that the materials investigated in this study does not fall under the precise definition of high-entropy alloys, nor do we intend to explore the properties and factors relating to high-entropy stabilized alloys such as the configurational entropy, phase stability and finite temperature studies. However this study is motivated from the discovery of these materials and promising properties, and venture into a more hypothetical space of materials, enabled by the computational methods available to study the potential properties of such materials. On the other hand, very recent studies **Mari, and other HEA silicide study** have experimentally synthesized high-entropy disilicides, thus in some way justifying the direction of this project.

We begin this project by reviewing key concepts of solid-state physics for readers lacking a background in materials science, and an introduction to the base 3d silicides of the experimental work. Later follows a theoretic walk-through of the relevant concepts of this thesis, these topics include high-entropy alloys, special quasi-random structures, and density functional theory. Next we shine light on the implementation of DFT in this project, and other computational details required to reproduce the results in this thesis, such as the use of the Vienna Ab Initio Simulation Package (VASP) and implementation of SQS. Finally we present the results of our study, these include the band gap and electronic properties of various structures and the success and challenges of the computational methods applied throughout the study.

Part I

Theory

Part II

Methodology and Implementation

Part III

Results and Discussion

Change this introduction to fit the final product! In this one year long project, we have collected results of a great number of materials with various structures and compositions. The initial experimentation was based on high-entropy silicides of the Fe_2Si unit cell, created from the special quasi-random structure approach as described above. Despite the non-semiconducting character of this compound, we worked under the idea that the extraordinary properties that have been observed in high-entropy alloys through effects such as the cocktail effect, we could discover specific combinations of elements that would yield a semiconductor. In addition, the ratio between silicon atoms to metals allowed us to create nearly equimolar high-entropy alloys.

Following this attempt, we transitioned into studying high-entropy silicides based on well known semiconducting 3d silicides such as β -FeSi₂, CrSi₂ and MnSi_{1.75}. The main outcome of this project is that for all 4 different starting silicides, we could only produce high-entropy silicides from one unit cell, furthermore in this cell only one specific compositions of elements was semiconducting. This was Cr_{0.25}Fe_{0.25}Mn_{0.25}Ni_{0.25})Si₂, here-in CFMN, in the β -FeSi₂ crystal structure.

This section will be structured in the following manner, firstly we will investigate the CFMN (fesi2) compound and various permutations of the composition. Thereafter we will look at other possible compositions of fesi2 based high-entropy silicides, and lastly test the CFMN composition in other crystal symmetries. In final we will present an overview of the complete study and the various compounds that have been investigated in order to propose promising directions and guideline future research directions in this field. In this way, we aim to understand the unique properties of CFMN (fesi2) and why this particular compound is semiconducting compared to the other testes structures in this project. Properties we will cover is the overall stability by total energy and corresponding enthalpy of formation, the magnetic properties and which elements contribute to the magnetism. But in majority, we will look at the band gap and related properties, as this is the main motivation and distinction of the study.

Add figure DOS FeSi2?

Chapter 7

The results of eqvimolar (CrFeMnNi)Si₂ in the β -FeSi₂ structure

β -FeSi₂ in the orthorhombic cmce crystal lattice is a well known semiconductor with an experimentally measured band gap of around 0.85 eV at room temperature [1], the nature of the band gap is under debate, all though most ab initio studies point to an indirect gap, experimental work indicate a direct gap. From our calculations we find an indirect band gap close to 0.65 eV with PBE, compared for example materials project's listed value of 0.698 eV with the same functional. Moreover in agreement with the calculations of materials project we discover that bulk β -FeSi₂ is diamagnetic. Finally, the enthalpy of formation of this compound is calculated as -18.6583eV .

The high-entropy alloys generated from the FeSi₂ unit cell alloys can be seen in figure 6.1. The supercells consist of 48 atoms each, in which the 16 iron sites is occupied equimolarly between Cr, Fe, Mn, and Ni, and the 32 silicon sites is as before occupied by silicon. Bellow in table 7.1 we list the total energy per atom (Toten), final magnetic moment (Mag) and band gap (E_G) of the five distinct SQSs, plus the mean and standard deviation (std) of the set, and enthalpy of formation ΔH of the mean energy. For simplicity we denote the 5 supercells as A, B, C, D and E.

SQS	Toten (eV)	Mag (μ_B)	E_G (eV)
A	-6,6080	0.0833	0.0280
B	-6,6138	0.0833	0.0523
C	-6,6063	0.0834	0.0344
D	-6,6155	0.0833	0
E	-6,6089	0.0833	0.0495
Mean	-6.6105	0.0833	0.0328
Std	0.0039	0.0000	0.0210
ΔH	-11.5000 eV	-	-

Table 7.1: Total energy per atom, final magnetic moment and band gap of 5 unique SQS of (CrFeMnNi)Si₂ based on the β -FeSi₂ unit cell.

From a first glance it's a clear distinction between the SQSs, especially in terms of the band gap and less so for the total magnetic moment. On the grounds of the total energy we note that the most stable supercell is SQS D, and reversely the least stable is SQS A. The band gaps listed in table 7.1 point to that the large majority of the SQSs are narrow-gap semiconductors in the range 0.028 - 0.052 eV, but the utmost stable configuration D does not exhibit any finite band gap.

In terms of the magnetism we see that contrary to the bulk FeSi₂ compound that this alloy is magnetic. Investigating the local magnetic moments of SQS D we discover that the ferromagnetic iron and nickel contain very small moments and non-existent in Ni. On the other hand the anti-ferromagnetic elements chromium and manganese contain large magnetic moments. In section 2.2 we provided several examples where Cr was known to reduce the saturation magnetization of high-entropy alloys. For example in the ferromagnetic HEA CoFeMnNiX, X = Al, Cr, Ga, Sn, studied in [2]. Mn had minimal impact on the magnetism and favoured the ferromagnetic phase, meanwhile addition of Cr pushed the material to a paramagnetic phase. Likewise in the equimolar system of CrMnFeCoNi [3], the local magnetic moment of Cr was found to align antiferromagnetic, and the ferromagnetic character was attributed to local magnetic moments of Fe and Mn. The odd magnetic properties experienced in this alloy can be related to several factors. Firstly are the limitations mentioned previously about both DFT and special quasi-random structures to model magnetic and particularly paramagnetic materials. Further the magnetic investigation and focus in this project have been very superficial with only considering non-spin polarized calculations or co-linear spin polarization, thus the phases in-between have been neglected. Lastly only the the ground state, ie 0K have been studied. Hence the reported magnetic properties should be taken with a grain of salt and are intended for subsequent studies focused on the magnetic properties of this alloy especially at non-zero temperatures.

7.1 The band gap

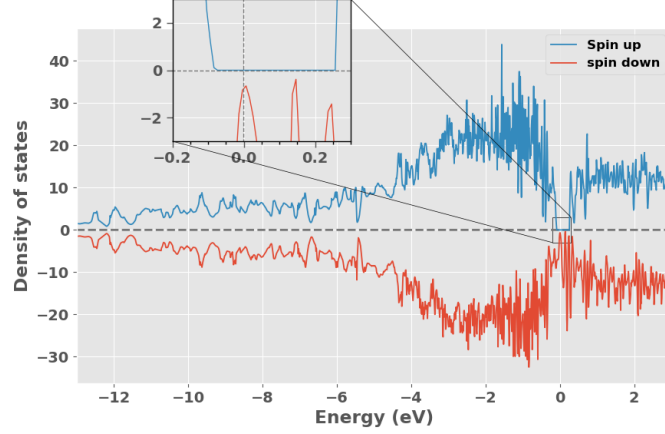


Figure 7.1: Density of states of SQS D (CrFeMnNi)Si₂ with PBE.

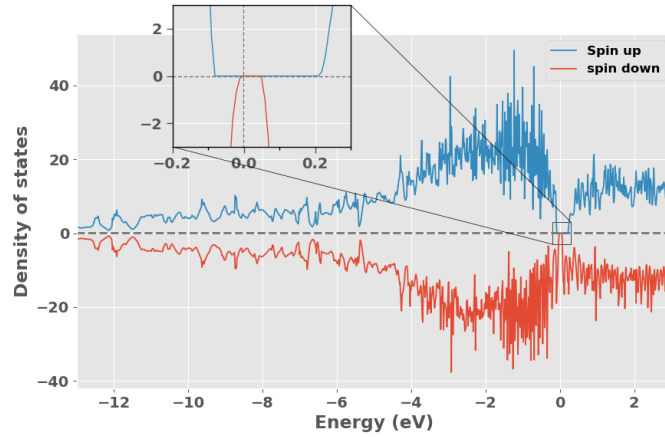


Figure 7.2: Density of states of SQS B (CrFeMnNi)Si₂ with PBE.

Above we plot the electronic density of states of SQS D and B from calculations with the PBE GGA functional. These supercells and corresponding properties are emphasized due to the relative stability in the set. Being the most stable means it's the most representative structure of the potentially "real" material, and hence so are the properties of that SQS. From the DOS in figure 7.1 we discover that the structure is in fact a half-metal with a band gap around 0.3 eV in the spin up channel and a metal in spin down. The exact value of the band gap in spin up is calculated from the range of energies corresponding 0 density of states around E_F , ie $0.2\text{eV} - (-0.1\text{eV}) = 0.3\text{eV}$. Following the total band gap of the solid is determined by the minimum range of energies from both spins, which in this case is 0 from the spin down DOS. Since these values are calculated by the density of states they will be denoted as $E_G^{\text{up}, \text{dos}}$ and $E_G^{\text{dw}, \text{dos}}$ to indicate the spin direction. By the

same mannerism we can see from figure 7.2 that the second utmost stable SQS (B) clearly contain finite values of both $E_G^{\text{up}, \text{dos}}$ and $E_G^{\text{dw}, \text{dos}}$. Similar figures can be seen for SQS A, C, and E in appendix ..., all respective spin dependent band gaps is listed below in table 7.2.

These values are determined from the calculated eigenvalues, and hence will be referenced to as $E_G^{\text{up}, \text{eigen}}$ and $E_G^{\text{dw}, \text{eigen}}$. This value is found by subtracting the highest energy eigenvalue in the valence band from the lowest energy eigenvalue in the conduction band. Across all five SQSs we observe in accordance with the magnetic property a distinction between spins where $E_G^{\text{up}} > E_G^{\text{dw}}$.

SQS	$E_G^{\text{up}, \text{eigen}}$ (meV)	$E_G^{\text{dw}, \text{eigen}}$ (meV)	$E_G^{\text{tot}, \text{eigen}}$ (meV)
A	81.4	52.2	28.1
B	293	52.2	52.2
C	236	34.3	34.3
D	339	0.00	0.00
E	308	50.0	50.0

Table 7.2: Band gap of the 5 SQSs of (CrFeMnNi)Si₂ calculated from the eigenvalues in spin up, down and total.

Alike the bulk material, these gaps are indirect. It would have been instructive to visualize and analyze the energy bands by plotting the band structure. Unfortunately this is neither simple to perform or interpret in large supercells consisting of several elements and a large number of energy bands. One solution is to do band-unfolding, but given the complex structure and implementation of the special quasi-random structures method in VASP this proved too challenging for the scope of this project.

A key point regarding the band structure of SQS D is the presence of defect states. In this structure the highest occupied conduction band is 128 for spin up states and band 124 in spin down, thus a difference of 4 bands between spins. For the spin down states we find that the highest energy conduction band, ie 124 have states with occupancy both slightly bellow 1.00 and above at several k-points. Likewise the lowest energy valence band (124) have partially filled states above 0.00 and bellow. The case of occupancy either above or bellow completely full or completely empty is simply a numerical inaccuracy well-known to calculations that apply the Tetrahedron method with Bloch corrections and have no real impact on the results. The second case where we have partially filled eigenstates in the conduction band and not completely filled states is a familiar term in random alloys [4] in which the forbidden energy gap is contaminated by defect states. To further study this effect we introduce $E_G^{\text{eigen}}(\text{occ})$ to represent the band gap calculated at a cut-off occupancy in the eigenvalues such that $E_G^{\text{eigen}}(0.99)$ only consider eigenstates with

occupancy above 0.99 as filled. Equivalently $E_G^{\text{eigen}}(0.01)$ only consider eigenstates with occupancy less than 0.01 as empty. In the following results we will list the occupancy parameter as a single value, such that $occ = 0.1$ represent occupancy equal to $1 - 0.1$ and $0 + 0.1$. Applying this to SQS D we get the results listed below in table .., keep in mind that $E_G^{\text{up, eigen}}$ is constant from that the defect states are only present in the spin down channel.

occ	$E_G^{\text{up, eigen}}$ (meV)	$E_G^{\text{dw, eigen}}$ (meV)	$E_G^{\text{tot, eigen}}$ (meV)
0.5	339	0	0
0.05	339	21.0	21.0
0.01	339	49.6	49.6
0.001	339	73.3	73.3
<0.0001	339	85.7	85.7

Table 7.3: Band gap of SQS D as a function of occupancy in the eigenvalues.

By including a threshold value to the occupancy and calculate the eigenvalue band gap at certain thresholds we find that the band gap increase as we neglect more defect states. Thus we may conclude that the band gap of SQS D or lack there of is attributed to the defects. Comparing to the density of states band gap plotted in figure 7.1, it's apparent that E_G^{dos} correspond to $E_G^{\text{eigen}}(0.5, 0.5)$, thus the density of states show the band gap with all defect states present.

7.2 Local and projected density of states

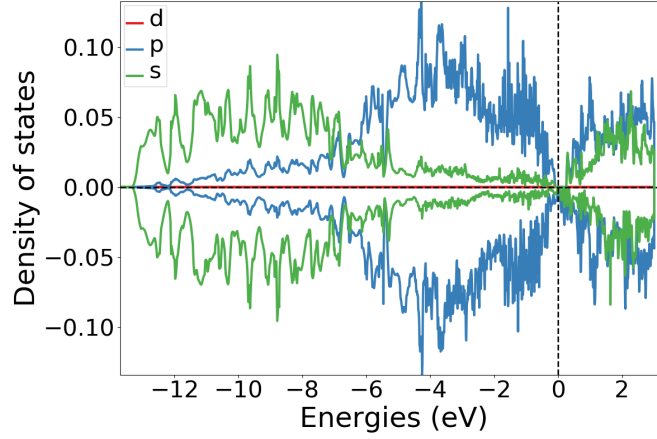


Figure 7.3: Local density of states of Si (SQS D)

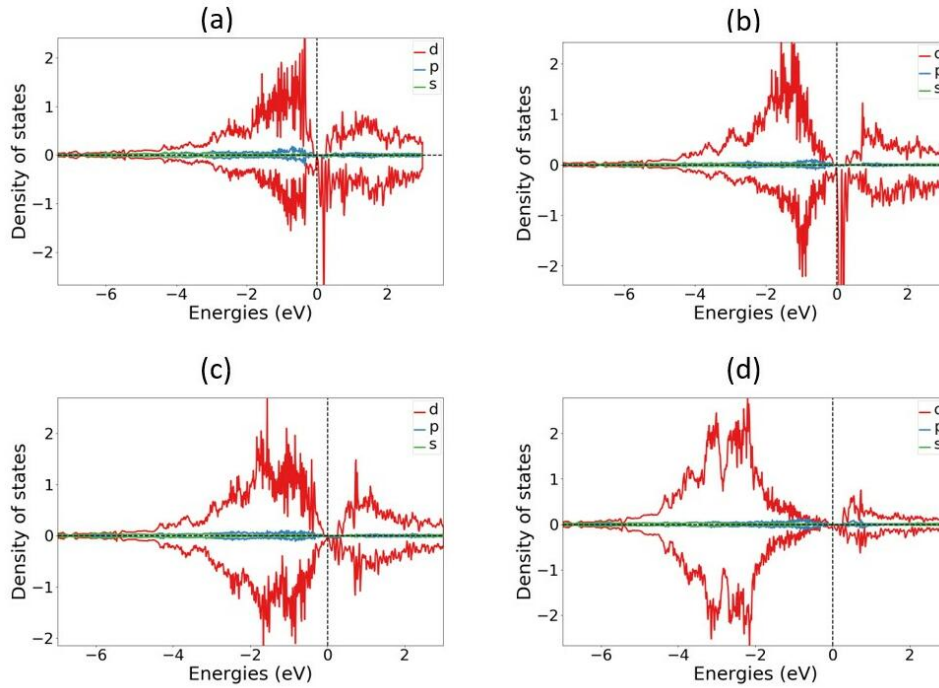


Figure 7.4: Local density of states of (a) Cr, (b) Mn, (c) Fe, (d) Ni in SQS D.

In the local density of states plotted in figure 7.3 we see that the s-electrons in Si occupy states in the lower energy regions and p electrons at slightly elevated energies closer to the Fermi energy, above E_F states are occupied by both s and p electrons almost equally. Further, the local density of states of the transition metals chromium, manganese, iron and nickel in SQS D is displayed below in figure 7.4. In spin down, manganese is most dominant especially above E_F , but also below E_F . Likewise chromium show a strong

presence above the Fermi energy in spin down. Both iron and Nickel show largest contribution at energies further from the Fermi energy, most notably below E_F . In the spin up channel we see a similar trend where chromium lies closest to E_F followed by manganese then iron and lastly nickel at the lowest energies. Another interesting observation is that the LDOS of iron and nickel is much more symmetric between spins, than Cr and Mn. Comparing to the LDOS of iron and silicon in bulk β -FeSi₂ [5] we find good agreement for both Fe and Si in this alloy.

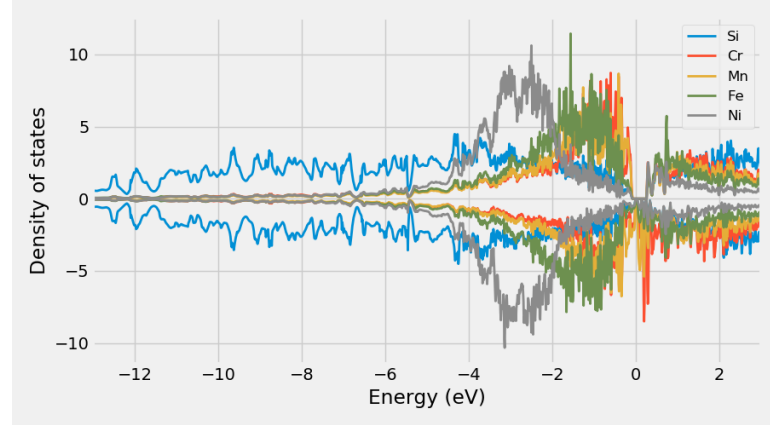


Figure 7.5: Projected density of states SQS D CFMN (fesi2) from PBE calculation

Moreover the relative positions and interplay between 3d elements and silicon as shown in the projected density of states (figure 7.5) is in good agreement with observed trends in simpler Si-rich transition metal silicides [6]. The electronic structure tends to be dominated by TM d electrons, and the valence band density of states are filled by non-bonding d states near E_F . The p-d hybridization between Si and TM elements typically falls about 6 eV below E_F and Si s states about 10 eV below. In our case we find that the Si states are pushed up closer to the Fermi energy by random alloying of various 3d elements.

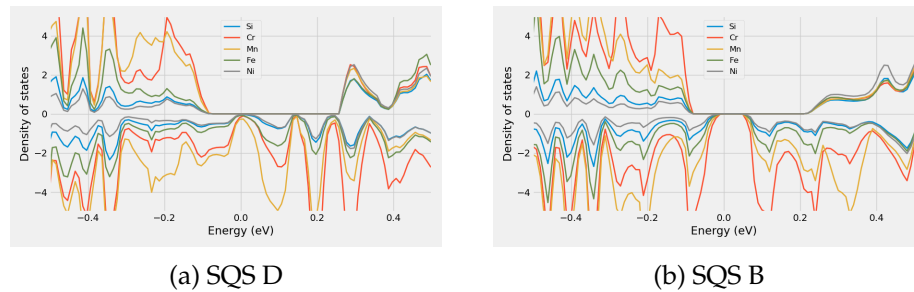


Figure 7.6: Projected density of states of SQS D and B around E_F

Above we have included the PDOS of SQS D and B but focused around E_F , from these figures we find that the spin down channel in D contains a more dominant presence of manganese especially, and some chromium as

compared to the semiconducting SQS B.

7.3 Results from SCAN and HSE06 functionals

As expressed previously in this work we invoke 3 level of depths GGA (PBE), meta-GGA (SCAN) and hybrid functional (HSE06) to determine the band gap of the SQSs, these results are showcased in table 7.4. Note that we do not specify eigen/dos or the occupancy here, because par SQS D the eigenvalues does not contain defect states, hence $E_G^{\text{eigen}}(0.5) = E_G^{\text{dos}}$.

SQS	XC-functional	E_G^{up} (eV)	E_G^{dw} (eV)	E_G^{tot} (eV)
A	PBE	0.0815	0.0521	0.0281
	SCAN	0	0	0
	HSE06	0.7084	0.0261	0.0261
B	PBE	0.2932	0.0523	0.0523
	SCAN	0.1470	0.0890	0.0890
	HSE06	0.2855	0.1819	0.1819
C	PBE	0.2355	0.0343	0.0343
	SCAN	0.0690	0.1124	0.1124
	HSE06	0.1744	0.0328	0.0196
D	PBE	0.3386	0	0
	SCAN	0	0.1086	0
	HSE06	0.3780	0	0
E	PBE	0.3078	0.0495	0.0495
	SCAN	0.1540	0.1112	0.1048
	HSE06	0.5476	0.0133	0.0133

Table 7.4: Band gap calculated with PBE, SCAN and HSE06 XC-functionals of (CrFeMnNi)Si₂ SQSs.

Aside SQS A, all 3 functionals agree on the presence of the band gap, but the exact size of the band gap is under debate. We report the largest total band gap to be associated with the SCAN functional, compared to PBE this is expected considering the factors mentioned in section .. about the limitations of generalized gradient approximations. In contrast, by the same argument we would not expect that par SQS B, to find the overall lowest band gaps from the well-proven hybrid functional HSE06. Nevertheless we observe generally good agreement between PBE and HSE06 calculations, with both producing large E_G^{up} and small or zero in the case of SQS D E_G^{dw} . In contrast as illustrated in figure 7.7 for SQS E (a + b) and D (c + d), SCAN enlarge the spin down value and decrease the spin up band gap in E and B, and further reverse the spin polarization of the band gap in SQSs C and D. Regarding SQS A, we find that the SCAN result suffers from defect states as was described previously for D, neglecting

said states yield $E_{G,SCAN}^{up,eigen}(0.99,0.01) = 0.0316$ eV and $E_{G,SCAN}^{dw,eigen}(0.99,0.01) = 0.0531$ eV resulting in a total gap of 0.0316 eV. Comparing to table 7.3 this appears to be in better agreement with particularly PBE, still however we find also here the same inverse spin polarization with SCAN.

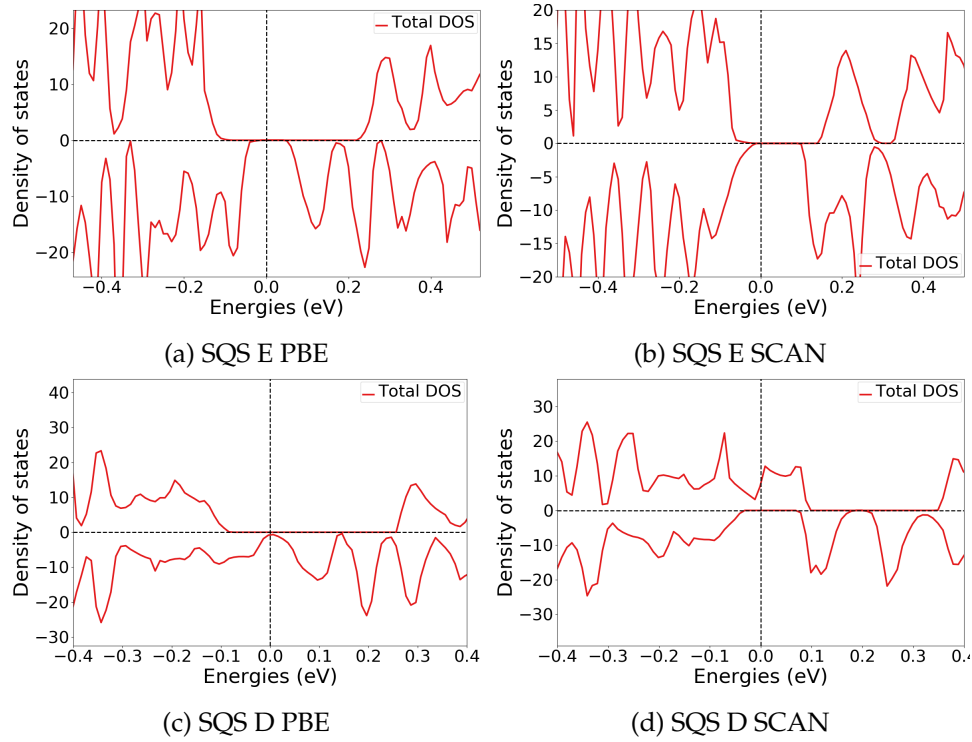


Figure 7.7: Density of states illustrating the band gaps from PBE and SCAN calculations for SQS E and D.

As stated above, HSE06 and PBE calculations yield mostly similar characteristics of the band gap. Looking at the spin dependent band gaps however it's clear that HSE06 in show large deviation to PBE, for example enlarged values in $E_{G,A}^{up}$, $E_{G,B}^{dw}$, $E_{G,E}^{up}$, or reduced values in $E_{G,A}^{dw}$, $E_{G,E}^{dw}$. And in other cases find nearly identical values to PBE as in $E_{G,B}^{up}$ and $E_{G,C}^{dw}$, or in SQS D that find excellent agreement in both spins. Generally we find that utilizing the HSE06 functional for these structures result in comparative or enlarged band gaps in spin up and lower values in spin down, with the exception of SQS B where HSE06 predicts a sizable band gap in both spins. Analog to the other cases, the 0 gap in D from HSE06 originates from defect states in the band structure, we get a band gap $E_{G,HSE06}^{dw,eigen}(0.99,0.01) = 0.2665$ eV from increasing the cutoff occupancy.

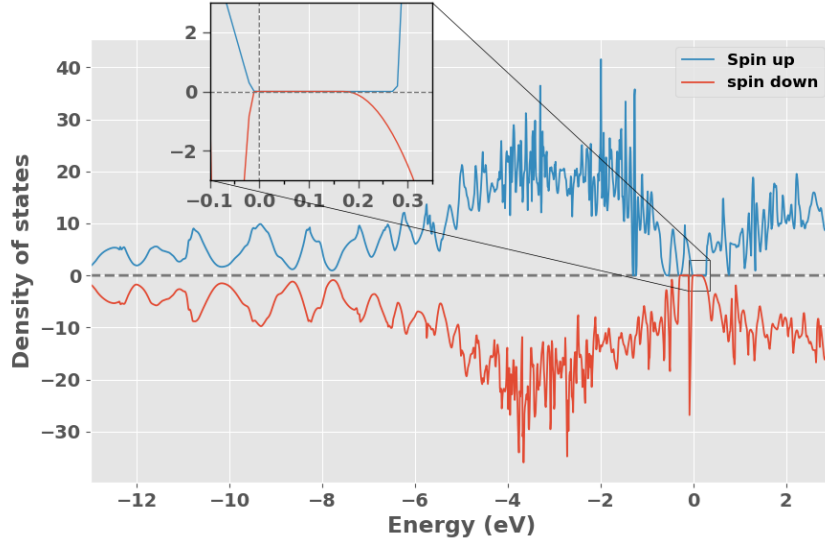


Figure 7.8: Density of states of SQS B with HSE06

The hybrid functional as expressed in section .. is computationally demanding to implement, in figure .. we show the computational cost in terms CPU-hours between PBE, SCAN and HSE06. One of the reasons behind the large cost of HSE06 is that we had to perform two subsequent calculations, firstly with Gaussian smearing and then secondly with TBC reapplying the calculated charge density. Nevertheless the CPU time of the first HSE06 calculation is still significantly greater than that of meta-GGA and GGA. Moreover the HSE06 calculations was performed with halve the number of k-points to PBE and SCAN in order to reach electronic convergence. Thus a completely justified comparison would contain even greater differences.

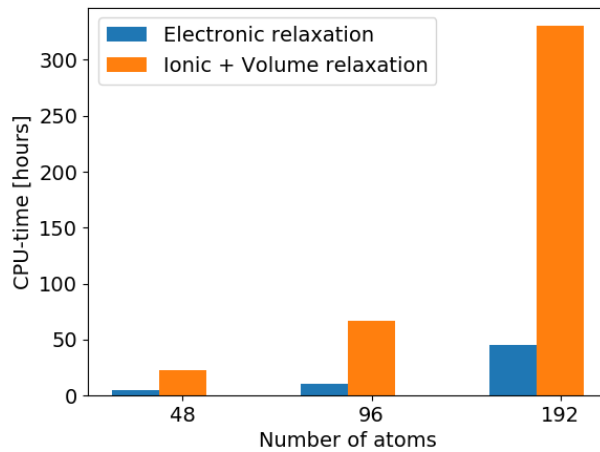


Figure 7.9: Something

The narrow mesh of k-points in HSE06 calculations is an important

factor to mention in relation to the HSE06 band gaps, that could lead to artificially exaggerated band gaps as the low density of k-points could fail to encapsulate the exact minimum transition between the valence band and conduction band. As seen in table 7.4 below the band gap is found between differing k-points from applying the 3 distinct functionals in SQS B (same in other SQSs).

XC-functional	Transition (k-point)
PBE	(0.250,0.000,0.250) \rightarrow (0.000,0.000,0.000)
SCAN	(0.250,0.000,0.250) \rightarrow (0.000,0.333,0.000)
HSE06	(0.500,0.000,0.000) \rightarrow (0.000,0.000,0.000)

Table 7.5: Minimum gap between k-point in valence band and conduction band in SQS B from PBE, SCAN and HSE06

The most concerning factor is that the highest energy k-point in the valence band from PBE calculations (0.250, 0.000, 0.250) is not considered in the HSE06 calculation with the narrow grid of 2x2x2 k-points. Thus one may suspect that the HSE06 calculation overlook the minimum transition and hence return an enlarged band gap. This could for instance be the case in $E_{G,A}^{up}$ and $E_{G,B}^{dw}$ where HSE06 predicts much larger values compared to PBE. However without an experimental baseline of the structure, we can not conclude that this is the case. As in the other SQSs we find examples where HSE06 produce similar or lower values than PBE despite applying the same number of k-points.

The numerical smearing is another important factor of the HSE06 calculations. In table 7.4 we list the outputs from using Gaussian smearing with smearing width *sigma* equal to 0.05 eV and 0.005 eV, and the tetrahedron method. Firstly we make note of that the Gaussian smearing at larger smearing width results in defects in the band gap and that neglecting these result in enlarged values most notably in spin down. Reducing the smearing width produces results in much better agreement with TBC. There are however a couple of exceptions, firstly $E_G^{up,eigen}$ of SQS A is in better agreement between TBC and gaussian with large smearing width. Reducing σ produces a lower band gap if 0.2 eV compared to around 0.7 eV in the other two. Furthermore $E_G^{dw,eigen}$ is enlarged to 0.10 and 0.12 eV from Gaussian in SQS A and E compared to 0.025 eV and 0.013 eV by TBC. The same is also the case in SQS D where we locate a small band gap in spin down with gaussian smearing. **SQS D low sigma in queue.**

SQS	Smearing (type) width (eV)	$E_G^{up,eigen}$ (0.5) (eV)	$E_G^{dw,eigen}$ (0.5) (eV)	$E_G^{up,eigen}$ (0.99) (eV)	$E_G^{dw,eigen}$ (0.01) (eV)	$E_G^{tot,eigen}$ (0.5) (eV)	$E_G^{tot,eigen}$ (0.99, 0.01) (eV)
A	Gaussian (0.05)	0.7837	0.1493	-	0.2984	0.1493	0.2984
	Gaussian (0.005)	0.2117	0.1013	-	-	0.1013	-
	TBC	0.7084	0.0261	-	-	0.0261	-
B	Gaussian (0.05)	0.2783	0.1702	0.2988	0.3136	0.1506	0.2979
	Gaussian (0.005)	0.2838	0.1823	-	-	0.1801	-
	TBC	0.2855	0.1819	-	-	0.1807	-
C	Gaussian (0.05)	0.1078	0.1066	0.2405	0.1839	0.0650	0.1839
	Gaussian (0.005)	0.1304	0.0222	-	-	0.0222	-
	TBC	0.1744	0.0328	-	-	0.0196	-
D	Gaussian (0.05)	0.3661	0.0592	-	0.1872	0.0592	0.1872
	Gaussian (0.005)	ND	ND	ND	ND	ND	ND
	TBC	0.3780	0	-	0.2665	0	0.2637
E	Gaussian (0.05)	0.6653	0.1439	-	0.1675	0.1439	0.1675
	Gaussian (0.005)	0.5825	0.1211	-	-	0.1211	-
	TBC	0.5476	0.0133	-	-	0.0133	-

Table 7.6: Band gap from HSE06 calculations with gaussian smearing and smearing width σ equal to 0.05 and 0.005, and the tetrahedron method (TBC). "-" mean unchanged values, "ND" means not done.

Below in figure 7.10 we plot the electronic density of states of with $\sigma = 0.05\text{eV}$, $\sigma = 0.005\text{eV}$ and the tetrahedron method of SQS ... **Hør med OML om disse resultatene**

Something something TBC is considered superior for precise total energy and density of states calculations of semiconductors [7], likewise TBC is inapt to simulate the forces in metals. **Examples?** However the impact of smearing was less noticable in GGA calculations of the band gap **examples, conclusion**

As a conclusion on the discussion of exchange-correlation functionals and the band gap of the $(\text{CrFeMnNi})\text{Si}_2$ high-entropy silicide, the fact that all 3 functionals and five SQS in majority agree on the presence of a band gap is in itself an overwhelmingly positive result that allow us to state with high certainty that this hypothetical materials is in fact a semiconductor, or possibly a half-metal based on the results of the utmost stable SQS D. An additional point to this is that as covered in great detail in literature on first principles studies, the PBE functional underestimate the value of a band gap. For example in this project we determine the band gap of bulk $\beta\text{-FeSi}_2$ with PBE calculations to around 0.65 eV compared to the experimental value of 0.85 eV. For this reason any values of the band gap with PBE would with high probability be replicated/increased in the real material. Compared to the nonmagnetic bulk material we find these alloys to yield sensible results, here we create a random alloy that as known will introduce defect states and hence lower the band gap and further make the material magnetic. We observe that this is most apparent in spin down as the the spin up gap is more comparable to the values of the parent FeSi_2 structure. In the next section we will look at the probability distribution functions before considering factors related to the special quasi-random methods in section 7.5.

7.4 Pair distribution functions

The probability distribution functions of SQS D and E can be seen below in figure 7.10, the PDFs corresponding to the remaining SQSs can be found in appendix .. . We include the PDFs of SQS D and B because as stated D is the most stable atomic configuration and hence the most representative of a potential real compound, and B to investigate distinctions between the half-metallic structure D and the semiconducting B which with HSE06 yielded substantial band gaps in both spins, recalling also that this is just very slightly below D in terms of stability. In the analysis we will put special emphasis on the nearest neighbor interactions since these are the most crucial in deciding the functional properties of a material.

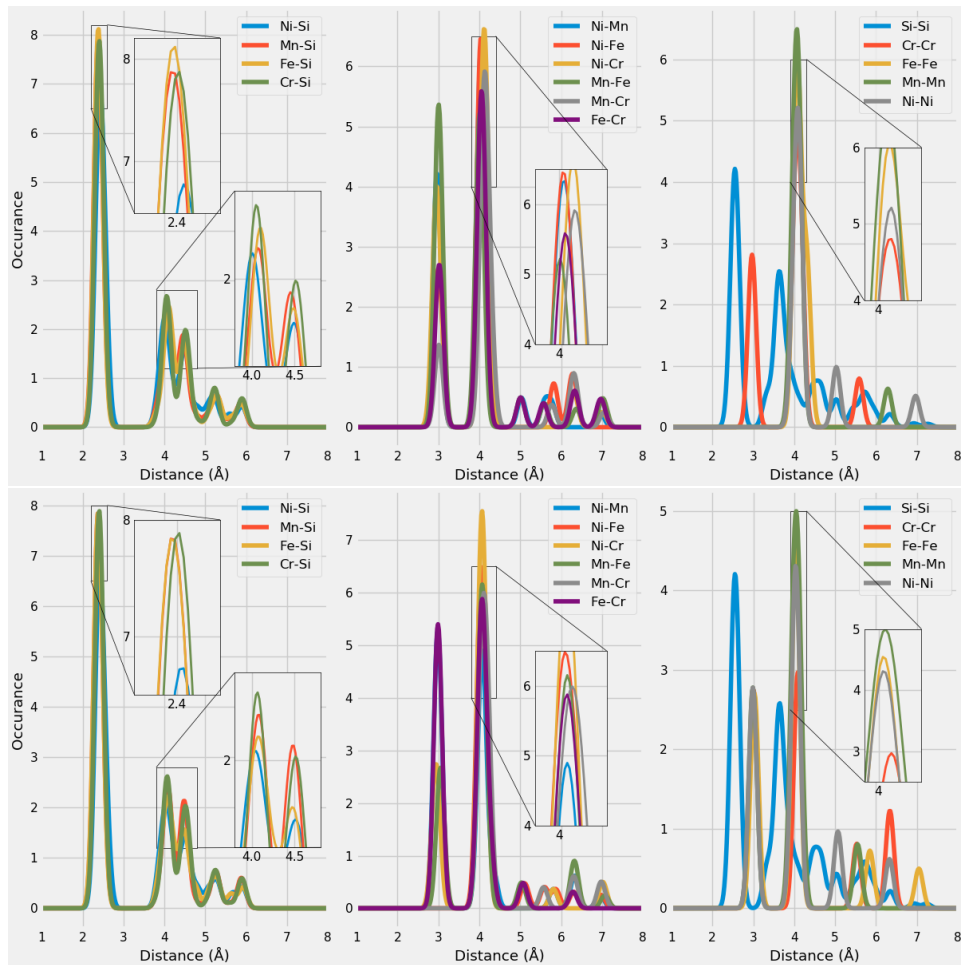


Figure 7.10: Probability distribution function of SQS D (top) and B (bottom)

We see that the relative positions of the PDFs remain consistent though both SQSs. With the aid of the ICSD (insert citation), we can compare the figure .. to the expected PDFs based on a number of experiments from a host of different compounds. As our compound contain a total of 15 different bonds, comparing each one to the ICSD values would be an exhaustive process. For our purpose we are satisfied by comparing the 4

different metal-Si bonds. We find that the preferred bond-length of TM-Si is observed at two values, the most dominant being the shorter of the two. For Fe-Si these are between 2.25-2.75 and 4-5, Mn-Si 2.25-2.75 and 3.5-5. Ni-Si lie between 2.25-2.5 and 3.85-5 and Cr-Si between 2.35-2.65 and 4-5. Clearly, the PDFs of the alloys are in good agreement with the listed values for Tm-Si bonds, with the most occurring bond length falling at around 2.4 Å for all TMs, and lesser occurrence between 4.0 - 4.5 Å. The height of the respective peaks is somewhat consistent in both structures, other than slightly reduced Fe-Si occurrence at 2.4 Å in B.

In contrast to the TM-Si bonds, we observe several distinctions between metal bonds in SQS D and B. Covering all would be tedious and not to insightful, instead we emphasize the bonds of Mn and Cr as this is where we found the biggest discrepancy in the PDOS. From the different TM-TM bonds (middle) of figure 8.8 we observe that the Mn-Fe bonds are most occurring at short distances in D and bigger distances in B, meaning that manganese and iron atoms are placed further from each other in structure D. **correct?** Similarly the bonds between Cr and Fe indicate that these atoms lie closer in B than D. In contrast the nickel and manganese/chromium bonds point to a closer distance in B for Ni-Mn and Ni-Cr in D, and a greater distance between Ni and Mn in D and Ni and Cr in B. **Litt kronglete kanskje?** In terms of the homogeneous bonds, the properties of both Cr-Cr bonds and Mn-Mn bonds are more or less alike in both structures besides some majority at shorter distance in D (The red Cr-Cr line at 3 Å is underneath the grey Ni-Ni line in B in figure 8.8 (bottom right)). A more significant distinction is that both Ni-Ni and Fe-Fe bonds are found at 3 Å and 4 Å in B, but exclusively 4 Å in D.

Both the Fe-Fe and Ni-Ni bonds are in better agreement with the ICSD histograms, as the most occurring distance for these bonds are between 4-4.9 Å and additionally around 2.5 Å. **More comparisons to ICSD, ask O.M.** As a conclusion on the PDFs of this compound, we locate a pattern where the Si-Si bonds are identical and only very minor differences between TM-Si bonds in SQS D and B. This is a result of how the structures are generated with the SQS method. In the FeSi₂ structure the silicon atoms are placed as before in the new supercells, but the TM elements are "randomly" distributed. Thus, it's reasonable that also here we would find the major differences between SQSs in the PDFs.

7.5 SQS size

Above we have presented the results of a high-entropy silicide (CrFeMnNi)Si₂ investigated by 5 48 atom SQSs with a volume of 700Å³. This intermediate size allowed for the use of more complex XC-functionals, and secondly enabled a broad study of distinct permutations and compositions as we will discover in the next chapters. However the application of the special quasi-random structures method to HEAs is not necessarily straightforward. Recalling from section 4.3 the first initial concern is the size of the SQS model and if it's sufficient enough to correctly model the disordered multi-component structure. In this section we will consider this problem by studying the difference between the 48 atom SQS to that of a 96 and 192 atom SQS with volume 1200Å³ and 2400 Å³ respectively. In figure 7.11 we plot the reported CPU time in hours between the 3 SQS sizes, which follows roughly a N^3 dependence.

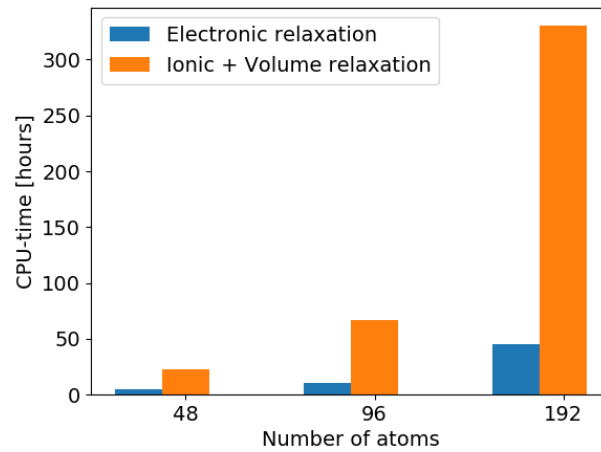


Figure 7.11: CPU time, **Make log plot instead**

Bellow we list the mean and standard deviation of the total energy, magnetic moment and enthalpy of formation of the 3 sizes in table 7.6, and band gaps in table 7.7.

SQS size	Toten (eV)		Mag (μ_B)		ΔH (eV)
	mean	std	mean	std	mean
48 atoms	- 6.6105	..	0.0833	0.0000	-11.5000
96 atoms	- 6.6092	0.0021	0.0708	0.0114	- 22.8752
192 atoms	- 6.6123	0.0022	0.0761	0.0171	- 46.6654

Table 7.7: Overivew 48, 96 and 192 SQSs.

As seen from table 7.4 both the total energy and magnetism remain

more or less consistent throughout all sizes, this is a good indication of that the 48 atom model can adequately model the alloy. **Something on the formation enthalpy.** The band gap as seen in table 7.7 is first of all evident across all 3 SQS models and show similar polarization favoring the spin up direction. In several cases, we find that the magnitude of the band gap lessen with increasing SQS size.

SQS size	SQS	$E_G^{up,eigen}(0.5)$ (eV)	$E_G^{dw,eigen}(0.5)$ (eV)	$E_G^{tot,eigen}(0.5)$ (eV)
48 atoms	A	0.0815	0.0521	0.0281
	B	0.2932	0.0523	0.0523
	C	0.2355	0.0343	0.0343
	D	0.3386	0	0
	E	0.3078	0.0495	0.0495
96 atoms	A	0.1705	0.0442	0.0367
	B	0.1386	0.0270	0.0270
	C	0.1347	0.0363	0.0075
	D	0.0892	0.0398	0.0398
	E	0.1610	0	0
192 atoms	A	0.1197	0.0321	0.0321
	B	0.1444	0	0
	C	0.1867	0	0
	D	0.0478	0.0339	0
	E	0.0131	0.0184	0.0131

Table 7.8: Band gap of SQSs of 48, 96 and 192 atoms each of (CrFeMnNi)Si₂. The names are arbitrary, ie A in 48 does not equal A in 96 or 192.

Similar to structure D in the 48 atom SQS we find that the 0 value in SQS E in the 48 atom model suffers from defect states and find $E_G^{dw,eigen}(0.90,0.10) = 0.016$ eV. The same is true for SQS B and C (192), but require $occ = 0.999, 0.001$ to locate a small nonzero spin down band gap. The band gap in SQS D and E (192) on the other hand is finite at $occ = 0.5$ but can be enlarged from increasing occ . In D we get $E_G^{up,eigen}(0.99) = 0.075$ eV and $E_G^{dw,eigen}(0.01) = 0.05$ eV and similarly $E_G^{up,eigen}(0.99) = 0.05$ eV, and $E_G^{dw,eigen}(0.01) = 0.048$ eV in E. In such cases where the eigenvalues inclusive of defect states return a finite band gap, the density of states does not. This is seen in figure .. for SQS E (192).

Drawing any conclusion on the band gaps is difficult seeing as we find very different results within the all 3 sizes. Based solely on the most stable SQS it's clear that the larger cell produce a much lower and different band gaps compared to the moderate SQS sizes which are much more similar. However also here we find that the gap in the 96 cell is only about half of the 48 atom cell. However as seen in table 7.7 we also find evidence of large band gaps in the larger cells in other atomic configurations. This goes back

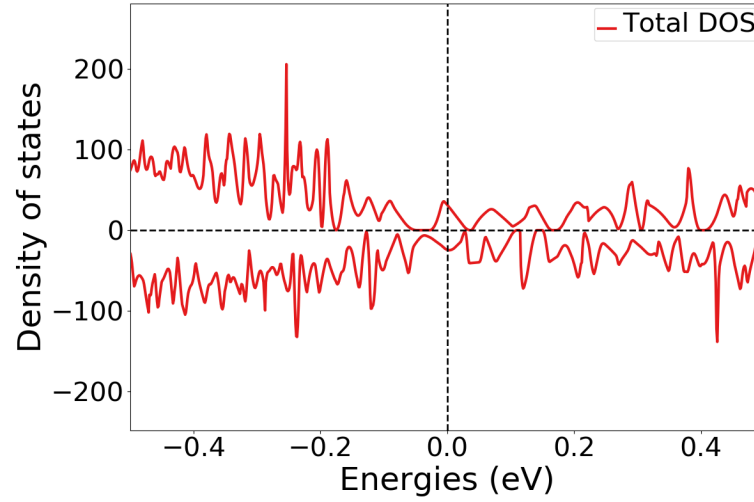


Figure 7.12: Density of states of SQS E 192 atom SQS.

to section .. when we mentioned that one of the biggest drawbacks of the special quasi-random structures method is the large number of possible atomic configurations, thus in order to conclude between results in this project the most sensible point is to consider the most stable SQS, but as seen from the very varying properties between SQSs of the same model, this does not necessarily been the most stable SQS if we trialed 20 SQSs instead of just 5. An additional point is the magnetic property, here we only applied one configuration to base the stability on, thus it's very probable that fine tuning the magnetic moments could result in different properties.

Looking at the pair distribution functions in figure 7.11 we see that the local ordering and short-range interactions is well represented and identical across all three sizes. The distinctions of preferences could as stated above simply be a product of the uniqueness of the SQSs more so than the size. On the other hand the larger SQSs clearly provide a better description of large-range interactions, that is not nearly as present in the smaller cell. However as seen in table 7.4 and in accordance with the fundamental concept of the special quasi-random structures method is that the functional properties is mostly determined by short-range effects in the lattice. Therefore, even though the bigger SQSs is a more accurate model the improvement is not justified from the cost, as illustrated in figure 7.12. And the apparent larger concern from applying the SQS method in this project is the uniqueness of each SQS.

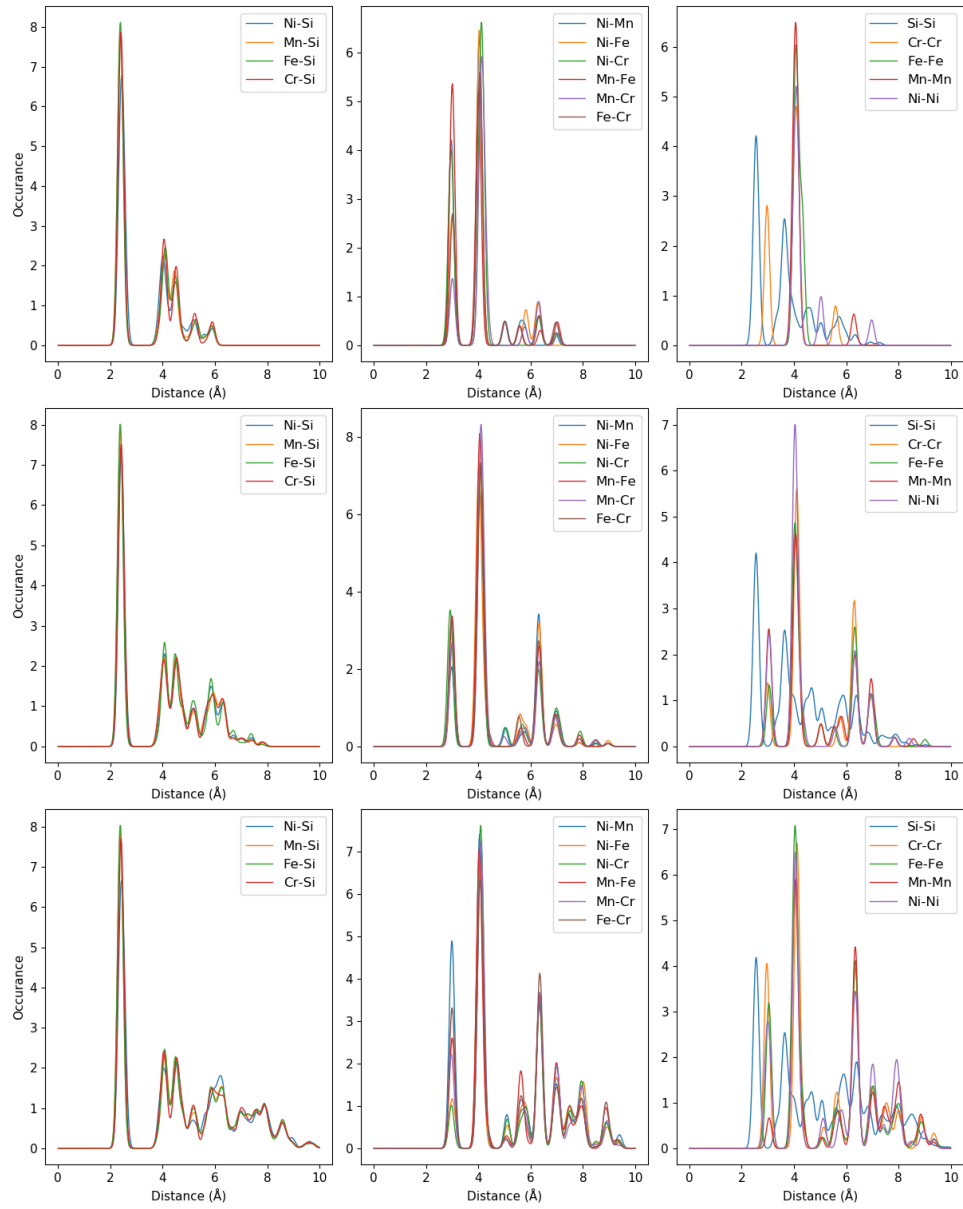


Figure 7.13: Pair distribution functions of SQS sizes (top) 48 atoms, (middle) 96 atoms, (bottom) 192 atoms

Chapter 8

Permutations of (CrFeMnNi)Si₂

Up until this point we have looked in detail at the high-entropy silicide (CrFeMnNi)Si₂ and associated SQSs. However these structures are just the center of a larger quasi-ternary phase diagram consisting of the different possible distributions of elements. Thus there exists many other compositions of this particular high-entropy silicide. In this section, we aim to expand our search of this diagram by generating SQSs of the 48 atom model slightly away from equimolar distribution of 3d elements. In table (bellow) we list the mean total energy and magnetic moment per atom with standard deviation and the enthalpy of formation of 4 compositions of the (CrFeMnNi)Si₂ alloy. Ideally they would differ only by one element, but the TDEP implementation insist in also reducing Nickel to stay consistent with the 48 atom supercell.

Composition	Toten (eV)		Mag μ_B		ΔH (eV)
	mean	std	mean	std	mean
Cr ₃ Fe ₃ Mn ₇ Ni ₃ Si ₃₂	- 6.6947	0.0040	0.1375	0.0186	-11.9586
Cr ₅ Fe ₅ Mn ₃ Ni ₃ Si ₃₂	- 6.6705	0.0030	0.1127	0.0223	-11.1991
Cr ₅ Fe ₃ Mn ₅ Ni ₃ Si ₃₂	- 6.6852	0.0041	0.1375	0.0456	-10.5200
Cr ₃ Fe ₅ Mn ₅ Ni ₃ Si ₃₂	- 6.6801	0.0036	0.0937	0.0209	-12.6426
Cr ₃ Fe ₃ Mn ₃ Ni ₇ Si ₃₂	- 6.3921	0.0078	0.0159	0.0101	-10.9614

Table 8.1: Summary composition diagram

The first result of table .. we make notice of is that the stability, as evaluated by the enthalpy of formation can be increased beyond the eqvimolar composition. This is accomplished in two distinct permutations, one with increments to manganese relative to the other TM, and the other by reduction of chromium. Moreover the two respective permutations lie on the opposite side of the magnetic scale. The large magnetic moment of the manganese rich permutation and the low magnetic moment in the

chromium poor permutation is very much in line with the observations made in the previous section. Recalling that in the magnetic moment in the equimolar composition was largely attributed to manganese and chromium atoms in the lattice. Thus increments to manganese or reduction of chromium would following impact the magnetic moment as in the two permutations. For this reason, additionally the permutation $\text{Cr}_5\text{Fe}_3\text{Mn}_5\text{Ni}_3\text{Si}_{32}$ where the nonmagnetic elements is reduced and the magnetic elements are increased, is equally magnetic. We however find no direct relation between stability and magnetism as his particular permutation is the least stable. An important property of table 8.5 is that the listed values are the mean value of the observed property for 5 distinct SQSs of the same permutation. For example we notice that while the highest magnetic moment in the first permutation is associated with the most stable SQS (from total energy considerations), and the least stable supercell show the highest magnetic moment in $\text{Cr}_5\text{Fe}_3\text{Mn}_5\text{Ni}_3\text{Si}_{32}$. Hence again we find the uniqueness problem of the special quasi-random structures troublesome in regards to making rigid conclusions of our results.

In table 8.2 we list the respective band gaps of the different compositions calculated with the PBE functional. Only the GGA functional was applied in this case because the motivation is primarily to compare the results to the parent equimolar composition and thus including 3 times as many results to calculate and analyze unnecessarily complicate the process. Thus we base this comparison between the PBE results of the new compositions to the PBE band gaps of the equimolar compound. In these compositions we find strong indication of a half-metal with less frequent SQSs with a band gap in the spin down channel than the equimolar compound. In the spin up channel on the other hand several compositions show very similar values to the equimolar composition. Between the different compositions particularly those rich in manganese provide very encouraging results and compositions poor in Mn less so. In terms of the stability we a very encouraging results of both the $\text{Cr}_3\text{Fe}_3\text{Mn}_7\text{Ni}_3\text{Si}_{32}$ and $\text{Cr}_3\text{Fe}_5\text{Mn}_5\text{Ni}_3\text{Si}_{32}$ compositions, where the most promising properties is attributed to the utmost stable configurations. in $\text{Cr}_3\text{Fe}_5\text{Mn}_5\text{Ni}_3\text{Si}_{32}$ the most stable SQS (D) is a semiconductor with a band gap around 0.1 eV.

Composition	SQS	$E_G^{\text{up, eigen}}(0.5)$ (eV)	$E_G^{\text{dw, eigen}}(0.5)$ (eV)	$E_G^{\text{tot, eigen}}(0.5, 0.5)$ (eV)
$\text{Cr}_3\text{Fe}_3\text{Mn}_7\text{Ni}_3\text{Si}_{32}$	A	0.3390	0	0
	B	0.4745	0	0
	C	0.1342	0	0
	D	0.1950	0.0063	0.0063
	E	0.4211	0	0
$\text{Cr}_5\text{Fe}_5\text{Mn}_3\text{Ni}_3\text{Si}_{32}$	A	<i>0.003</i>	0	0
	C	<i>0.21</i>	0	0
	D	0.0674	0.0413	0.0372
	E	<i>0.362</i>	0	0
$\text{Cr}_5\text{Fe}_3\text{Mn}_5\text{Ni}_3\text{Si}_{32}$	A	0.2082	0	0
	B	0.4053	0	0
	C	0.4659	0	0
	D	0.0843	0.0121	0.0121
	E	0.3008	0	0
$\text{Cr}_3\text{Fe}_5\text{Mn}_5\text{Ni}_3\text{Si}_{32}$	A	0.3922	0	0
	C	0.1285	0	0
	D	0.2595	0.1004	0.1004
	E	0.3591	0.1003	0.0848
$\text{Cr}_3\text{Fe}_3\text{Mn}_3\text{Ni}_7\text{Si}_{32}$	A	0	0	0
	B	0	0	0
	C	0	0	0
	D	0	0	0
	E	<i>0.04</i>	0	0

Table 8.2: Band gaps of various compositions of $(\text{CrFeMnNi})\text{Si}_2$. Most stable SQS of a set is highlighted in bold text, band gap with defect states are listed in cursive. Some SQSs were excluded from the table due to unsuccessful calculations.

Below in figure 8.1 we plot the projected density of states around E_F of the first four compositions of table 8.2. Note that away from the Fermi energy the projected density of states is analogous to the parent equimolar composition. The below figures is based on the most stable SQS in each permutation, as will the analysis. Hence the features of these figures can be subject to the uniqueness of that particular SQS rather than a distinct feature of the exact composition, but as stated previously the most stable configuration provide the most likely properties of the composition within the scope of this project.

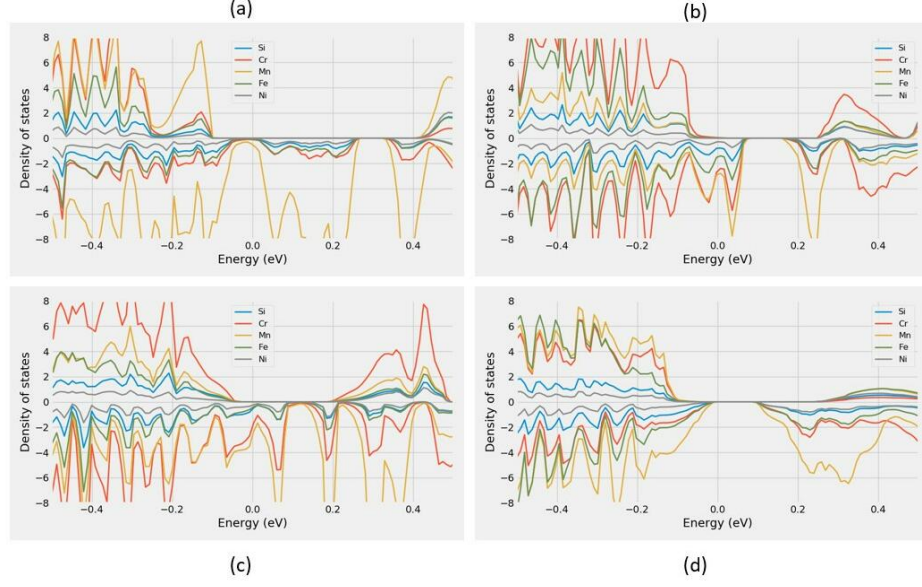


Figure 8.1: Projected density of states of (a) $\text{Cr}_3\text{Fe}_3\text{Mn}_7\text{Ni}_3\text{Si}_{32}$ (SQS B), (b) $\text{Cr}_5\text{Fe}_5\text{Mn}_3\text{Ni}_3\text{Si}_{32}$ (SQS C), (c) $\text{Cr}_5\text{Fe}_3\text{Mn}_5\text{Ni}_3\text{Si}_{32}$ (SQS A), (d) $\text{Cr}_3\text{Fe}_5\text{Mn}_5\text{Ni}_3\text{Si}_{32}$ (SQS D)

With that said, the plotted PDOSs in figure 7.1 is in good agreement with the listed values in table 7.2. $\text{Cr}_3\text{Fe}_3\text{Mn}_7\text{Ni}_3\text{Si}_{32}$ (7.1 a) and $\text{Cr}_5\text{Fe}_3\text{Mn}_5\text{Ni}_3\text{Si}_{32}$ (7.1 c) both indicate a sizable spin up band gap, further figure (7.1 d) point to a total band gap around 0.1 eV for SQS D of $\text{Cr}_3\text{Fe}_5\text{Mn}_5\text{Ni}_3\text{Si}_{32}$. On the other hand we find dissimilarity between the density of $\text{Cr}_5\text{Fe}_5\text{Mn}_3\text{Ni}_3\text{Si}_{32}$ SQS C and the eigenvalue band gap listed in table 7.2. In figure 7.1 d we find a range of forbidden energies slightly above the Fermi energy, and very small values in spin up at the Fermi energy. Similar to what we experienced in the 192 atom SQS in section 7.4, the eigenvalues report a finite band despite of defect states. Therefore the density of states is not completely zero at E_F .

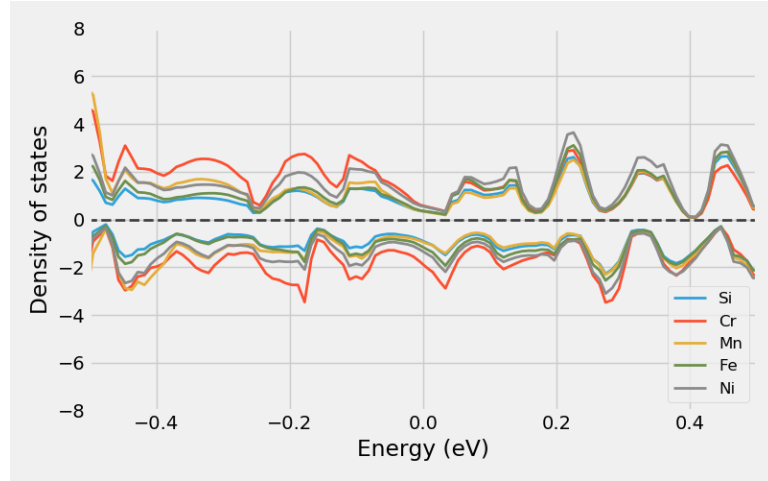


Figure 8.2: Projected density of states of $\text{Cr}_3\text{Fe}_3\text{Mn}_3\text{Ni}_7\text{Si}_{32}$ around E_F

In figure 8.6 we saw that electrons from manganese atoms in particular was a key contributor as to why the spin down channel of $(\text{CrFeMnNi})\text{Si}_2$ was metallic in the stable supercell D. This is also largely the case in the permutations shown above in figure 8.12. The proportion of manganese atoms in the alloy seems to offer a very positive effect on the band gap in spin up, but is often detrimental to spin down. This is seen in figure 8.12 (a) and (c) for $\text{Cr}_3\text{Fe}_3\text{Mn}_7\text{Ni}_3\text{Si}_{32}$ and $\text{Cr}_5\text{Fe}_3\text{Mn}_5\text{Ni}_3\text{Si}_{32}$ respectively, that both contain increased amounts of manganese. By reducing the number of Mn as in (b) we still find that the Mn electrons plague the states at E_F in spin down. In analog we see from (b) and (c) that also Cr negatively impacts to the band gap especially in spin up. The sole permutation with clear evidence of a spin down gap is from the chromium poor permutation plotted in (d). Also in this structure we see that the effects of Mn around E_F is dampened in comparison to the other permutations, despite containing relatively increased amounts of Mn to the eqvimolar alloy.

An important property of these results is that because each permutation alters simultaneous elements, interpreting and relating the results to a particular alteration is challenging. For example, is the result of the $\text{Cr}_5\text{Fe}_3\text{Mn}_5\text{Ni}_3\text{Si}_{32}$ permutation a consequence of less Fe or increments to both Cr and Mn? Furthermore is the large band gap in spin up of $\text{Cr}_3\text{Fe}_3\text{Mn}_7\text{Ni}_3\text{Si}_{32}$ a product of increasing manganese or reducing the other elements. From the comparatively large gaps in spin up of $\text{Cr}_3\text{Fe}_3\text{Mn}_7\text{Ni}_3\text{Si}_{32}$ and $\text{Cr}_3\text{Fe}_5\text{Mn}_5\text{Ni}_3\text{Si}_{32}$ and the more present Cr states in spin up in the Cr rich permutations we here conclude that the band gap is related to lessening of chromium, more so than other effects. However we see from both $\text{Cr}_5\text{Fe}_5\text{Mn}_4\text{Ni}_3\text{Si}_{32}$ and $\text{Cr}_3\text{Fe}_3\text{Mn}_3\text{Ni}_7\text{Si}_{32}$ (figure 8.2) in addition to the manganese rich composition that Mn plays a vital role on the band gap of these structures. It's clear that the $\text{Cr}_3\text{Fe}_5\text{Mn}_5\text{Ni}_3\text{Si}_{32}$ alloy manage to strike a balance between 3d elements that results in a specific interplay and correspondingly very promising properties.

Chapter 9

Different compositions and crystal structure

9.1 New compositions

In similar fashion to the previous sections, we here begin by presenting the mean and standard deviation of the total energy and magnetization of a set of SQSs corresponding to different high-entropy silicides of the FeSi_2 unit cell. The compositions we have tested are deliberate combinations intended to investigate both the impact of manganese by replacing the element with Co or Ti, and concepts related to HEA theory such as the atomic size effect. Furthermore Co is a very common element in many stable HEA, as seen in section 2.2, thus we include 3 compositions with Co to study the impact on stability and the functional properties. The results of the aforementioned alloys can be seen below in table 9.1, note that all compounds contain a total of 48 atoms as before.

Composition	Toten (eV)		Mag (μ_B)		ΔH (eV)
	mean	std	mean	std	mean
$\text{Cr}_4\text{Fe}_4\text{Co}_4\text{Ni}_4\text{Si}_{32}$	- 6.4655	0.0056	0.0083	0.0155	- 12.7536
$\text{Co}_4\text{Fe}_4\text{Mn}_4\text{Ni}_4\text{Si}_{32}$	- 6.4731	0.0046	0.0000	0.0000	- 15.0836
$\text{Cr}_4\text{Fe}_4\text{Ti}_4\text{Ni}_4\text{Si}_{32}$	- 6.4217	0.0087	0.0305	0.0293	- 7.5040
$\text{Cr}_4\text{Fe}_4\text{Mn}_4\text{Ti}_4\text{Si}_{32}$	-6.6994	0.0071	0.1142	0.0641	- 7.3060
$\text{Cr}_4\text{Fe}_4\text{Mn}_4\text{Co}_4\text{Si}_{32}$	-6.7687	0.0034	0.1331	0.0326	- 13.7796

Table 9.1: Overview new compositions

From table 9.1 we see that the stability of the relative compositions vary greatly. By introducing cobalt to the alloys, particularly at the cost of manganese result in a large positive effect on the stability, contrary replacing either manganese or nickel with titanium significantly lowers the stability. **Wait for new formation enthalpies.** In table 9.1 we have listed the mean magnetic moment of the compositions, in line with previous results

in this project the magnetization is very dependent on chromium and manganese. This is seen by the overall lowest magnetic moments in the two compositions without these elements, and reversely the highest magnetic moments is found for compositions with both Cr and Mn. Comparing the magnetic moment of $(\text{CrFeCoNi})\text{Si}_2$ and $(\text{CoFeMnNi})\text{Si}_2$ it seems in our study that chromium is most responsible for the magnetic moment in these alloys. Furthermore we find that substituting Ni with both Ti and Co result in more magnetic compounds. These are truly surprising results, one would expect that the magnetic moments would be larger in the ferromagnetic elements Ni, Fe and Co than Cr, Mn and Ti. This could go back to our simplistic and superficial study of the magnetic properties in this project, additionally the PBE functional as we covered in section .. have shown limitations for 3d elements and particularly Ni. Thus this could be a factor affecting our results. Another factor is that we here based our comparison on the mean values between 5 SQSs. As we have experienced throughout this project the uniqueness of the SQSs can be troublesome to handle, and our best guess is to study the most stable super-cell. Below in table 9.2 we list the magnetic moments of the most stable SQSs. Here we find several dissimilarities to the mean value such as the $\text{Cr}_4\text{Fe}_4\text{Co}_4\text{Ni}_4\text{Si}_{32}$ being nonmagnetic in the most stable supercell. Thus based on the utmost stable configurations we can state that replacing either Cr or Mn (with Co) removes the magnetic moment in the alloy. Furthermore we find from these supercells that the magnetic moment is reduced by replacing Ni with Ti, and increased from Co. These results are in much better accordance with previous knowledge of ferromagnetic elements and their interplay in high-entropy alloys.

Composition	Magnetic moment (μ_B)
$\text{Cr}_4\text{Fe}_4\text{Co}_4\text{Ni}_4\text{Si}_{32}$	0
$\text{Co}_4\text{Fe}_4\text{Mn}_4\text{Ni}_4\text{Si}_{32}$	0
$\text{Cr}_4\text{Fe}_4\text{Ti}_4\text{Ni}_4\text{Si}_{32}$	0,0653
$\text{Cr}_4\text{Fe}_4\text{Mn}_4\text{Ti}_4\text{Si}_{32}$	0,0785
$\text{Cr}_4\text{Fe}_4\text{Mn}_4\text{Co}_4\text{Si}_{32}$	0,1666

Table 9.2: Final magnetic moment of the most stable supercell of each composition.

In regards to the band gap of these compositions, we find most to be metals. The band gap of the most stable SQS of each composition is listed in table 4.3, where we calculate the band gap from the eigenvalues at different occupancy cutoffs. As before the 0 band-gap is caused by defect states in the band gap. By increasing the criteria, in other words only consider states with occupancy above a certain threshold, the band gap become finite at $occ = 0.1$ and converge to around 0.02 – 0.06 eV depending on composition, when only considering full/empty states.

Composition	occ	$E_G^{up, eigen}$ (eV)	$E_G^{dw, eigen}$ (eV)	$E_G^{tot, eigen}$ (eV)
CrFeCoNiSi ₂	0.5	0	0	0
	0.1	0.00095	0.0399	0.00095
	0.01	0.063	0.063	0.063
CrFeTiNiSi ₂	0.5	0.0067	0	0
	0.1	0.061	0.0087	0.0087
	0.01	0.061	0.037	0.037
CoFeMnNiSi ₂	0.5	0	0	0
	0.1	0.0037	0.0037	0.0037
	0.01	0.0268	0.0268	0.0268
CrFeMnTiSi ₂	0.5	0	0	0
	0.1	0.021	0.00049	0
	0.01	0.03	0.03	0.022
CrFeMnCoSi ₂	0.5	0.461	0	0
	0.1	0.607	0.0218	0.0218
	0.01	0.607	0.0245	0.0245

Table 9.3: Band gaps of the most stable SQS of β -FeSi₂ high-entropy silicide compositions as a function of occupancy in the eigenvalues.

The one exception to the metallic compositions is the CrFeMnCoSi₂ composition with a gap of around 0.5 eV in the spin up channel. As seen in previous cases, this structure despite of the large band gap contains also a small amount of defect states. This is seen in the projected density of states plotted in figure 4.1, where we observe small nonzero values of the density of states at the Fermi energy. The PDOSs of the other compositions is found in appendix ..

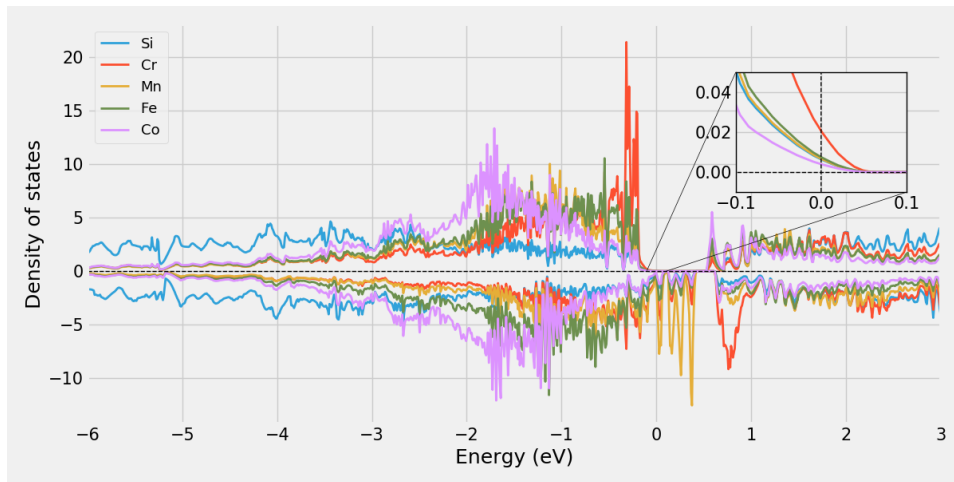


Figure 9.1: Projected density of states of (CrFeMnCo)Si₂.

Contrary to the above case, inserting Co in the place of manganese clearly result in a metallic structure, as seen in the density of states in figure 9.2 a. Replacing Mn with Ti instead we recall from table 9.3 a a very small defect band gap in spin up, however from figure 9.2b we observe that E_G^{dos} is equal to zero, thus $E_G^{dos} \neq E_G^{eigen}$. Comparing the density of states of $(\text{CrFeCoNi})\text{Si}_2$ and $(\text{CrFeTiNi})\text{Si}_2$ tha the latter is magnetic and the former nonmagnetic, as we discussed previously.

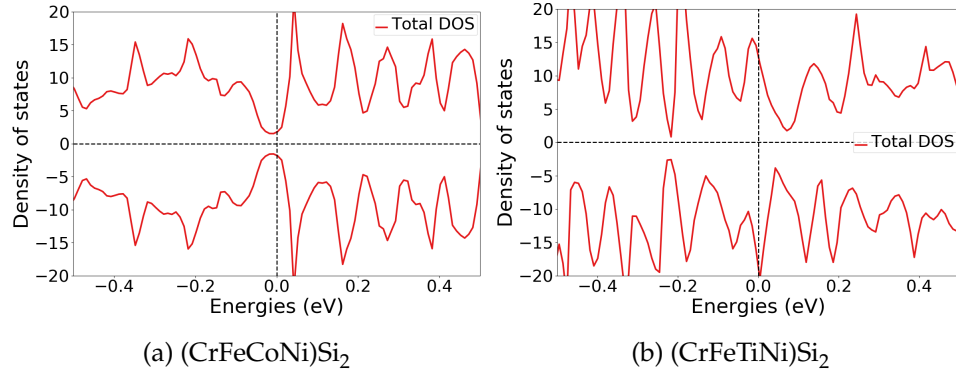


Figure 9.2: Density of states of a) $(\text{CrFeCoNi})\text{Si}_2$ and b) $(\text{CrFeTiNi})\text{Si}_2$.

Above we have looked at the band gap of the most stable SQS of each composition, but as we have experienced in other cases in this project, the properties can vary between SQSs of the same composition. In both CrFeCoNiSi_2 and CrFeMnTiSi_2 we found only metallic supercells with the exception of one SQS in the latter with a very small defect band gap in spin up. Similarly small defect band gaps was observed in two SQSs of CrFeTiNiSi_2 and the rest as metals. In CrFeMnCoSi_2 we found a large defect band gap in spin in the most stable configuration, here we find similar band gaps in two other SQSs as well, and two structures. The most interesting case was found in CoFeMnNiSi_2 where we observed small total band gaps without defect states in two SQSs, these are seen in figure 9.3. In agreement with the nonmagnetic character of this composition, the DOS is symmetric with respect to spins.

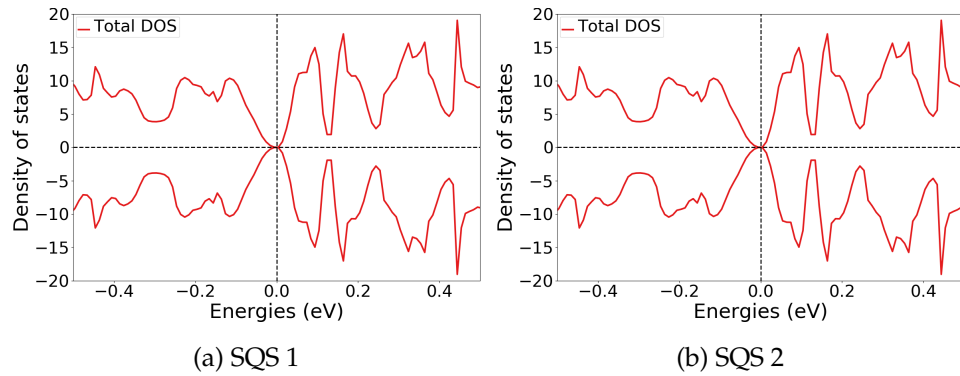


Figure 9.3: Density of states of two SQSs of $(\text{CoFeMnNi})\text{Si}_2$.

Thus we find examples where the most stable SQS is representative of the set, and other cases where we observe meaningful distinctions between the most stable and other possible configurations. Because of limited time examining properties and options affecting both the magnetism and stability of the alloys and respective supercells, it's important to consider the different configurations as a broader search would not necessarily yield the same relationship. **Can I say this?** It appears that we find limited success overall, but particularly when substituting either Cr or Mn as outlined in the previous section. Furthermore Ti is not as successful as Co. **Continue conclusion this and entire project**

Part IV

Conclusion

Write conclusion here

Bibliography

- [1] S. J. Clark et al. 'Structure and electronic properties of FeSi_2 '. In: *Phys. Rev. B* 58 (16 Oct. 1998), pp. 10389–10393. DOI: 10.1103/PhysRevB.58.10389. URL: <https://link.aps.org/doi/10.1103/PhysRevB.58.10389>.
- [2] Tingting Zuo et al. 'Tailoring magnetic behavior of CoFeMnNiX ($X = \text{Al, Cr, Ga, and Sn}$) high entropy alloys by metal doping'. In: *Acta Materialia* 130 (2017), pp. 10–18. ISSN: 1359-6454. DOI: <https://doi.org/10.1016/j.actamat.2017.03.013>. URL: <https://www.sciencedirect.com/science/article/pii/S1359645417302008>.
- [3] Oldřich Schneeweiss et al. 'Magnetic properties of the CrMnFeCoNi high-entropy alloy'. In: *Phys. Rev. B* 96 (1 July 2017), p. 014437. DOI: 10.1103/PhysRevB.96.014437. URL: <https://link.aps.org/doi/10.1103/PhysRevB.96.014437>.
- [4] Voicu Popescu and Alex Zunger. 'Effective Band Structure of Random Alloys'. In: *Phys. Rev. Lett.* 104 (23 June 2010), p. 236403. DOI: 10.1103/PhysRevLett.104.236403. URL: <https://link.aps.org/doi/10.1103/PhysRevLett.104.236403>.
- [5] R. Eppenga. 'Ab initio band-structure calculation of the semiconductor $\beta\text{-FeSi}_2$ '. In: *Journal of Applied Physics* 68.6 (1990), pp. 3027–3029. DOI: 10.1063/1.346415. eprint: <https://doi.org/10.1063/1.346415>. URL: <https://doi.org/10.1063/1.346415>.
- [6] H Lange. 'Electronic properties of semiconducting silicides'. In: *physica status solidi (b)* 201.1 (1997), pp. 3–65.
- [7] ISMEAR - Vaspwiki. URL: <https://www.vasp.at/wiki/index.php/ISMEAR>.